PREDICTION OF WELD-ABILITY CHARACTERISTICS OF DUAL-PHASE STEEL HCT600X BY NUMERICAL SIMULATION

EMIL EVIN[1*], JOSEF TEJC[2], MIROSLAV TOMAS[1]
VLADIMIR KOKARDA[3]

[1]Department of Automotive Production, Faculty of Mechanical Engineering, Technical University of Kosice, Kosice, Slovakia

[2]ESI Eastern Europe s.r.o, Plzen, Czech republic

[3]Carl Zeiss Slovakia, s.r.o, Bratislava, Slovakia

DOI: 10.17973/MMSJ.2024_11_2024014

E-MAIL Emil.Evin@tuke.sk

Abstract: Dual-phase (DP) steel plates are characterized by very good absorption capacity, so they are used in the automotive industry for body deformation zone parts. They are attached to the frame of the car-body by welding. Laser welding of dual-phase steels is gaining increasing importance in the automotive industry. In the present paper, the possibility of predicting the strength and deformation characteristics of laser-welded HCT600X steel sheets was analyzed based on experiments and numerical simulations. Butt joints were formed by YLS-5000 laser in two variants, which differ by laser power input and welding speed. The HCT600X- HCT600X with welded joint was analyzed based on microstructure and mechanical tests. The tensile strength and hardness of the welded joints were greater than those of the base material (BM). The microstructure of the weld metal (fusion zone) consisted of martensite, austenite and bainite, in the heat-affected zone it consisted of a mixture of martensite, bainite, ferrite and residual austenite. In numerical simulation, the finite-element mesh was created by linear volume elements refined in the weld region, and the Gauss model of the surface heat source was applied when modelling laser welding. The results of numerical simulation of the microstructure and selected mechanical properties were correlated with the experimental results.

KEYWORDS
laser welding, numerical simulation, phase composition, stress and strain distribution, distortion

1 INTRODUCTION

Today, the key to success is to produce at low cost, with high quality and within the time required to deliver the product to the market. The development of computer technology and numerical methods applied through CAE programs makes it possible to examine the characteristics of both the product and the technology of its production virtually already during its design and the design of the technology of its production design. This reduces the need to perform real experiments, prototyping or additional repairs, leading to significant cost savings. In the case of numerical welding simulation, there are several software (Ansys, Nastran, Simufact welding, Abaqus, ArcWeld, SYSWELD, Flow-3D Weld, Transweld) that allow advanced meshing techniques and various thermomechanical analyses, either as stand-alone software packages or integrated within CAD systems [Devaraj 2021, Danielewski 2020, Doshi 2020].

Using numerical welding simulations in SYSWELD, it is possible to predict: the distribution of thermal fields, the size of the heat affected zone (HAZ), the material structure in the weld metal (WM) and in the heat affected area, the hardness of the structure, residual stresses, strains, etc. On the basis of the obtained results, it is possible to perform the optimization of the welding technological procedure numerically so that the desired parameters of the welded joint are achieved without the need to perform real experiments. The basis of the welding simulation is a thermo-mechanical-metallurgical model [Kik 2020, Hilditch 2007].

The safety is one of the key factors that largely determines the success or failure of a given car concept. In terms of passive safety, a key role is played by the structure of the car body, whose deformation structure is designed to absorb as much kinetic energy as possible in a collision [Rusz 2019]. The ability to absorb impact energy is very closely related to the toughness of the materials. Among AHSS, two-phase steels are very often used by structural engineers for the parts of deformation structures [Stańczyk 2023].

Dual-phase steel consists of a soft ferritic matrix in which islands of martensite are dispersed [Alves 2018]. The combination of these phases gives the material very good fatigue resistance and toughness while maintaining good formability. The total martensite content in DP steels is in the range of 5-30%. As the proportion of the martensitic phase increases, the strength of the steel increases. DP steels are characterized by high values of strain-hardening exponent n and high EA of impact energy. Thanks to these properties, these steels allow the production of parts of deformation structures that are stronger and at the same time lighter, which creates prerequisites for reducing fuel consumption and emissions [Danielewski 2020], [Mansur 2021]. Dual-phase steel is produced in standardized quality generations DP350/600, DP 500/800, DP 600/980 [Beer 2020, Schmitt 2018, Xu 2016].

The use of deformation structure parts in the body structure is associated with their joining into assemblies. One of the processes used in joining body parts into complex assemblies is laser welding. During welding, the material will melt in the central area of the weld joint. Thus, the temperature in this area exceeds the melting temperature of the material and forms the fusion zone (FZ) and weld metal (WM). Because this region of the FZ is intensely heated and then intensely cooled, the micro-structure in the FZ is almost completely martensitic and its hardness is 1.5–2 times that of the base material [Moeinifar 2011], [Dong 2014]. In addition to martensite, ferrite and bainite can occur in this region [Correard 2016, Zhao 2013]. The hardness of FZ is closely related to the carbon equivalent of steel [Gao 2018].

A phase change occurs on both sides of the FZ due to heat transfer from the FZ. This area is referred to as the heat affected zone (HAZ). HAZ contain fine martensite and un-dissolved ferrite [Moeinifar 2011]. Depending on the welding parameters, a small amount of bainite may also be present in the HAZ [Farabi 2010]. Changes in the microstructure at the weld joint and the heat-affected zone can lead to catastrophic failures in automobile operation and collision [Alves 2018]. For this reason, the optimization of welding parameters based on the results of experimental research is of great importance. Then, these results can serve in the verification of numerical simulations. For designers, the prediction of strength and deformation characteristics is of great importance too. Because they enable them in a short time to verify different variations of welding procedures and their effect on the strength and

deformation properties of deforming body parts [Schindlerova 2024].

The aim of the paper is to present the applicability of the laser to welding of HCT600X dual-phase steel plates of nominal thickness 0.8 mm, to evaluate the effects of welding on the mechanical properties, on the microstructure of the welded joint and on the residual stresses and to compare them with the results obtained by simulation.

2 MATERIALS AND METHODS

2.1 Materials and Methods

The dual-phase steel sheets HCT600X were used for the experimental research and numerical simulation, chemical composition of which is presented in the Tab. 1 [Evin 2017, Švec 2018]. The volume fraction of martensite in the base material was ≈ 17 % and ferrite ≈ 83 %. In laser welding, the laser beam is very narrow compared to other fusion welding processes, so the weld surfaces must be aligned when welding. A larger distance between the joining specimens may be the cause of weld defects (no continuous weld joint formed, weld concavity, undercutting, notch appearance, etc.) [Hilditch 2007]. Thus, the specimens of 0.78 mm thick and 20 mm wide sheet metal were fabricated by electroerosion. The pairs of specimens prepared in this way were butt welded by YLS-5000 laser that has the following parameters: power 5000 W; wavelength 1.06 µm; an optical fiber diameter of 0.3 mm. Samples for experimental research were prepared by laser welding with the following parameters:

- variant V01 - laser power 2 kW, welding speed 50 mm/s,
- variant V02 - laser power 2.7 kW, welding speed 70 mm/s.

Welding parameters were optimized based on weld porosity, root quality and mechanical properties. As a more suitable (higher quality) weld joint, the joint was obtained at a laser power of 2.0 kW and a welding speed of 50 mm.s^{-1}. Fig. 1 presents the macrostructure of HCT600X weld joint. The total width of the weld joint is approx. 2 mm, the width of welded metal area is approx. 1.2 mm and the width of heat-affected area is approx. 0.4 mm. The localization of plastic deformation and failure of both the sample of the base material and the sample of the laser-welded material occurred outside the center of the samples – Fig. 2c.

C	Si	Mn	P	S	Cu	Al	Cr	Mo	Ni	V	Ti	Nb	Co	W
0.11	0.012	1.963	0.026	0.002	0.019	0.031	0.206	0.003	0.002	0.012	0.02	0.02	0.017	0.005

Table 1. Chemical composition of dual-phase HCT600X [wt %].

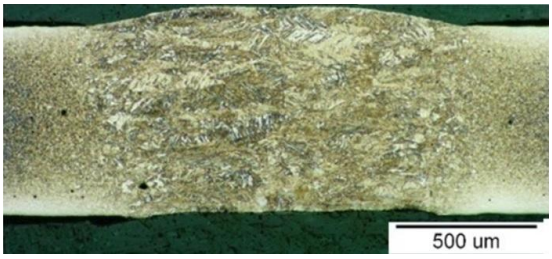

Figure 1. Macrostructure of laser weld of dual-phase HCT600X.

Experimentally determined values of mechanical properties are given in Tab. 2 [Evin 2017]. The mechanical properties (yield strength, tensile strength, uniform and total elongation, material constant *K*, strain-hardening exponent and plastic strain ratio) of the basic material and laser-welded strips were measured by standardized tests (ISO 6892-1, ISO 10113:2006 and ISO 10275:2007) on samples shown in Fig. 2, using the machine TIRAtest 2300 at the strain rate $\dot{\varepsilon} = d\varepsilon/dt = 0.0021\ s^{-1}$. Three specimens have been tested in 90° to the rolling direction.

Material	$R_{p0.2}$ [MPa]	R_m [MPa]	A_g [%]	A_{80} [%]	K [MPa]	n [-]	r [-]
BM	376	632	19	28	1096	0.217	0.77
LJ	435	677	17	20	1109	0.182	0.76

Note: BM – base material; LJ – laser joint.

Table 2. Mechanical properties of dual-phase steel HCT600X .

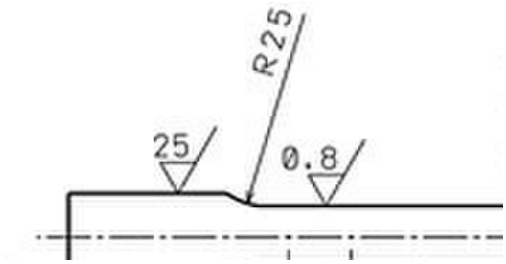

Figure 2a. Specimen shape and dimension for tensile test without weld.

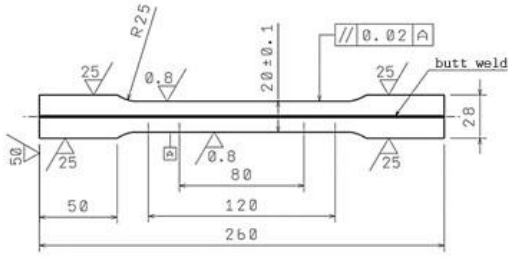

Figure 2b. Specimen shape and dimension for tensile test with laser joint.

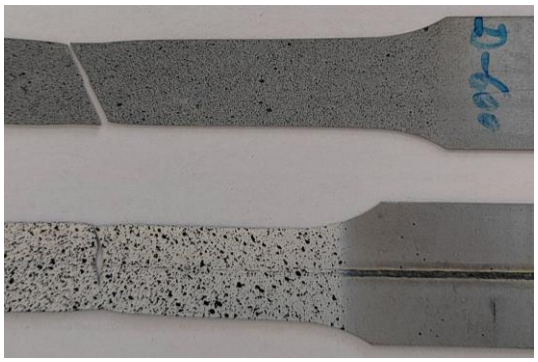

Figure 2c. Specimens after fracture – base material (top) and laser weld (bottom)

2.2. Numerical simulation of laser welding

The laser welding simulation was performed using the FEM solver SYSWELD. The software allows to simulate the processes of welding, heat treatment and subsequently also thermochemical treatments such as cementation,

carbonitridation, nitriding [1]. Simulation of the welding process requires the following analyses:

- thermo-metallurgical analysis,
- mechanical analysis.

A 3D Gaussian model is used for welding processes with high power density in the beam incidence area. Heat source calibration is performed based on actual process parameters and weld macrography. In the case of the SYSWELD solver, it was realized based on the definition of an equivalent heat source, which induced the same temperature field in the model as in this real weld.

When entering the heat source, the power input and welding speed were defined. It is assumed that in the considered laser welding process, a molten region with full penetration across the thickness of the sheet of width approx.1 mm arises. For both variants of the laser welding process, a conical heat source was used with the same characteristics of energy distribution and the expected efficiency of the process of 30% [Sokolov 2014, Bergman 2011]. A 3D sample model was created from the sheet of 0.78 mm thickness with dimensions of 20x40 mm (Fig. 3a), and it was subsequently discretized into a finite element mesh (Fig. 3b).

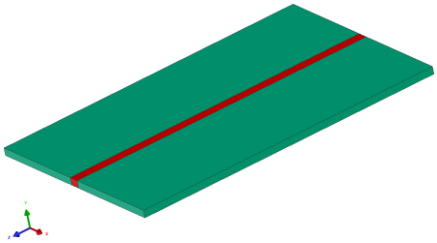

Figure 3a. Simulation model of laser welding process - specimen geometry.

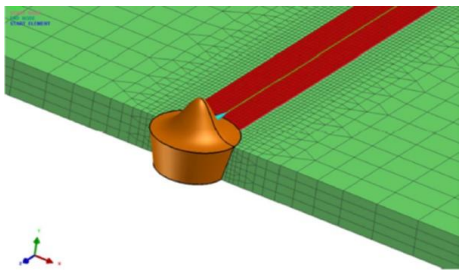

Figure 3b. Simulation model of laser welding process - geometry and energy distribution of the heat source.

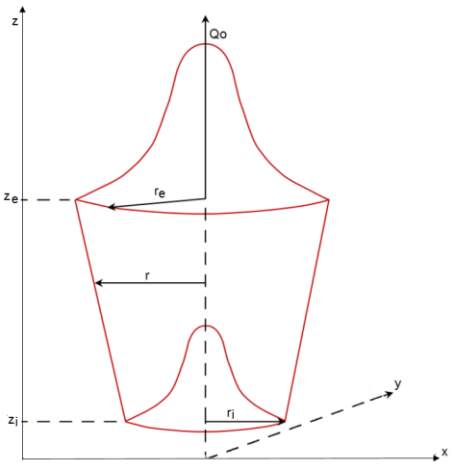

Figure 3c. Simulation model of laser welding process - heat source characteristics.

At welding processes simulation with high power density (laser welding, plasma and micro-plasma or electron beam) the Gauss model is applied (Fig. 3c). In the SYSWELD environment, the Gauss model of surface heat source is predefined [Kik 2020, Hilditch 2007]. Heat source with the 3D Gauss distribution of heat source can be determined using the relation (1):

$$q(x,y,z) = Q_0 \, exp\left(\frac{x^2 + y^2}{r_z^2(z)} \right) \quad (1)$$

where Q_0 is the heat flux density into material; $_{re}$, r_i are laser weld radii; and z_e, zi determine the re-melting deep of the laser weld.

The finite element mesh is made up of linear volumetric elements, mainly of hexa type, with a smaller part of penta type. Corresponding mesh refinement was performed in the weld area. The welding simulation was performed using the SYSWELD software. The external ESI Group database of the software contains mechanical properties (yield strength, Young's modulus, Poisson's coefficient and others) and thermometallurgical properties (standard specific heat, thermal conductivity, density, martensitic transformation temperatures: A_{c1} and A_{c3}) of the DP-W-600, which has an equivalent chemical composition (Tab. 1) to material DP 600. Thus, in the simulation, material data DP-W-600 (1.0936) from the program´s library was used.

In the numerical simulation, two parameters of heat source movement and laser power were set in the experiment: variant V1 - laser power 2.0 kW, welding speed 50 mm/s; variant V2 - laser power 2.7 kW, welding speed 70 mm/s.

The purpose of the boundary conditions in the welding simulation is to describe the thermal interaction of the model with the environment and to define the conditions of mechanical fixing of the sample, or the model positioning. It is assumed that the object is surrounded by an ambient atmosphere (air), a heat transfer coefficient considering heat losses by radiation and convection was defined. Boundary conditions were defined to represent rigid fixing of the specimen during welding and free cooling at five nodal points. Zero offsets were prescribed for the nodal points of the mesh on both sides of the model – Fig. 4a. This condition for fixing was removed in the last stage of the calculation and replaced by the condition of statically determined storage (combinations of 6 degrees of freedom were removed) – Fig. 4b. Thus, the final state of tension and deformation of the weldment after release from the fixture was obtained.

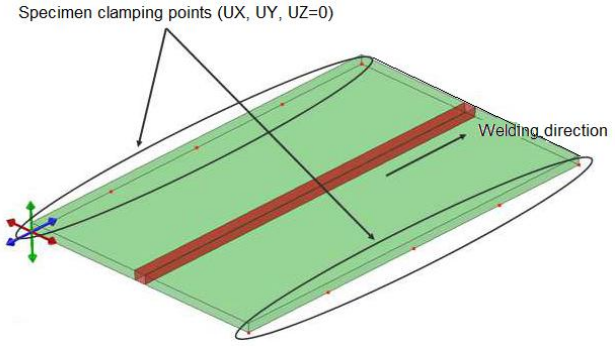

Figure 4a. Conditions of the specimen during laser welding - fixing the specimen during welding and cooling.

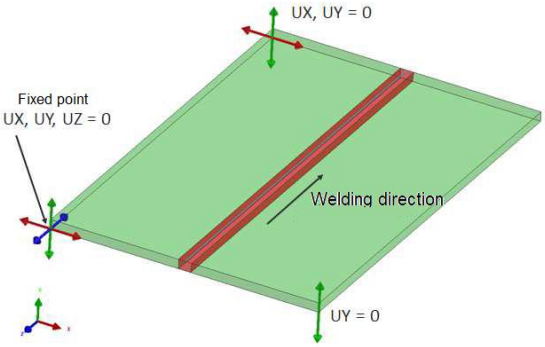

Figure 4b. The condition of statically determined specimen clamping at the end of the calculation.

3. RESULTS AND DISCUSSION

A large number of time states were the result of the computation during simulation when the heat source passed through the model and underwent subsequent cooling. The analysis was performed on the samples after cooling to room temperature and after their release from the fixture. The results were evaluated in a section perpendicular to the welding direction and positioned at the mid-length of the specimen model.

The values of the maximum temperatures reached are presented in Fig. 5 as a function of the relative distance from the edge of the model. The temperature curves indicate that in both cases the melting temperature was exceeded (V1: 2330 °C and V2: 2470 °C). After reaching the maximum, the temperature drops sharply. Due to the different welding speed, the heat source passes around the indicated point at slightly different times, which makes the comparison of the two temperature cycles somewhat complicated. The results obtained by simulation show a very similar situation in both computational variants in terms of the nature and penetration of the temperature fields around the welded joint. In Variant 2, a slightly "narrower" temperature field was achieved due to the higher power and welding speed, but in contrast, the maximum temperature directly in the center of the welded joint was slightly higher. It should be noted that the SYSWELD solver does not accurately describe the behavior of the molten material and the phenomena associated with the effects of the laser beam, therefore it is necessary to take into account the fact that the calculated values of the temperature profiles inside the molten region may not be completely accurate in terms of absolute values. Similarly, slightly higher heating and cooling rates can be observed in total for variant 2.

Fig. 6 shows the dependence of temperature on time in half of the sample. In this case the temperature is about 1000 °C, i.e. above A_{c3} (867 °C, according to the SYSWELD database). Thus, it is a state of complete austenitization in this region. The cooling rate in this case is lower than in the previous case. In the simulation, it is important to define the lowest temperature (A_{c1}) at which austenite can form and the temperature (A_{c3}) at which austenite transformation ends. The progression of the transformation of the individual phases as a function of the changing temperature at different cooling rates is plotted by the CCT. Above temperature A_{c1} (727 °C), partial austenitisation begins to take place. The residence time above A_{c1} is very short ($t_{8/5}$ was 0.09 s). At temperatures below A_{c1} no phase trnasformation occurs. At higher cooling rates, austenite is transformed to martensite. The transformation rate can also be greatly affected by the initial grain size due to the change in the surface area available for nucleation. From a comparison of the two temperature cycles, it can be seen that there is very little variation on the time axis as the heat source passes through a given point due to the different welding rates.
However, the aforementioned differences between these results are very small and, from a practical point of view, insignificant. Thus, very similar weld widths can also be expected – Figure 8.

The basic transformation of steels at temperatures above A_{c3} is the conversion of the initial ferritic-martensitic structure to an austenitic structure. If the cooling rate of the austenitized structure is high, then austenite is transformed to martensite. As a result of the transformation, thermal and deformation of the material in the welded joint area is affected.

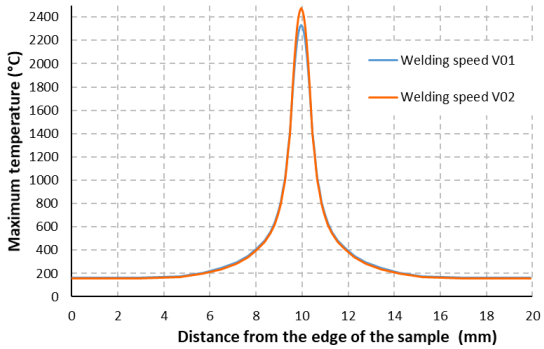

Figure 5. Course of temperature with respect to the edges of the sample.

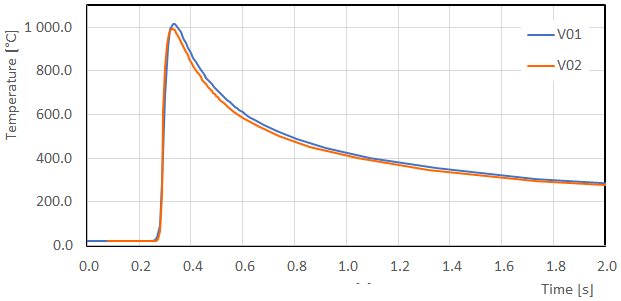

Figure 6. Comparison of thermal cycles at a selected point.

Since the local temperature in BM was below A_{c1} austenization did not take place and no change in structure occurred on subsequent cooling. The microstructure of the HCT600X base material is fine-grained polyhedral consisting of equiaxed ferritic grains and very fine martensite grains - Fig. 7a.

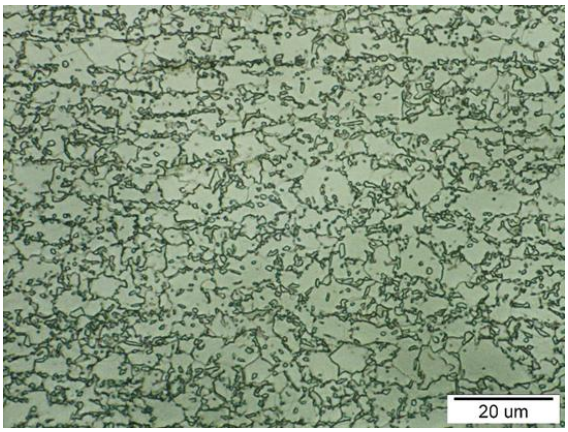

Figure 7a. Microstructure of base material of dual-phase steel HCT600X (BM).

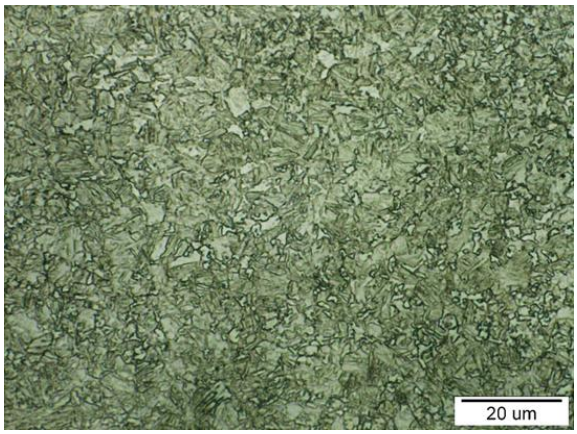

Figure 7b. Microstructure of two-phase steel HCT600X in the area of the heat-affected zone (HAZ).

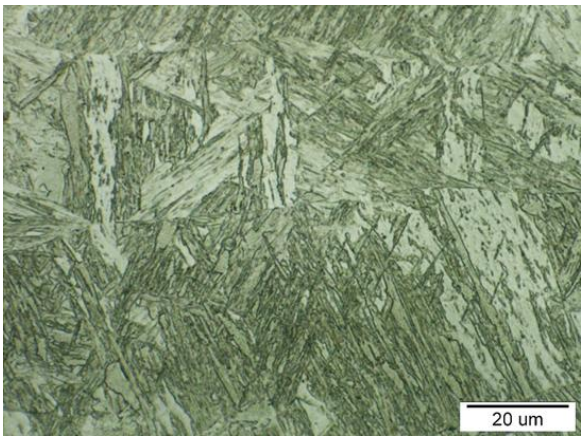

Figure 7c. Microstructure in the weld metal area of dual-phase steel HCT600X (WM).

However, there are visible lines in the distribution of phases in the structure and particles of impurities. It can be assumed that tertiary cementite is also present in the structure. In the transition region between BM and HAZ, tempering occurs, which in some cases causes softening of the structure, i.e., the hardness in this transition region is less than that of BM [Hilditch 2007]. The experimentally determined average hardness value in BM was about 207 HV0.5 and higher values of ≈ 10 HV0.5 were found by simulation for variant V1 - Fig. 8. The temperature in the heat affected zone was in the region between A_{c1} and A_{c3}. Towards the heat-affected zone, the orientation of the martensitic laths decreases, which is the result of the decrease in size and reduction in the orientation of the austenite grains in which the martensite was formed. This refinement of the martensite is visible in the heat-affected zone adjacent to the weld metal – Fig. 7b. The fine martensite found in the HAZ, fine grains of ferrite are also present, the proportion of which increases towards the BM. In the vicinity of BM the proportion of ferritic grains exceeds that of martensite. The experimentally found average hardness value in HAZ was ≈ 320 HV0.5. Higher hardness values were found by simulation in this zone, which reproduced the values found experimentally - Fig. 8. The temperature in the WM region was above A_{c3}. The microstructure of the weld metal is formed by lath martensite, which formed in elongated austenite grains - Fig. 7c. The experimentally found average hardness value in the WM was 388.6 HV0.5 for variant V1 and 387.4 HV0.5 for variant V2. In the numerical simualtions it was 393.6 for variant V1 and 393.1 for variant V2 – Tab. 3.

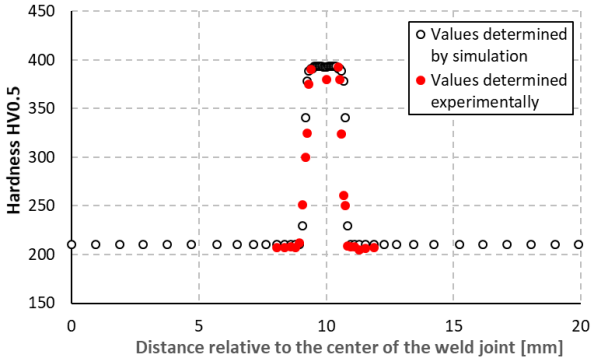

Figure 8. Comparison of hardness results found experimentally and by numerical simulation.

Power Speed		BM	HAZ 1	WM	HAZ 2	BM
2 kW 50 mm.s^{-1}	Avg	236	357	389	335	239
	Stdev	5	10	5	11	6
2.7 kW 70 mm.s^{-1}	Avg	238	317	387	320	239
	Stdev	14	7	14	13	12

Table 3. Microhardness HV0.5 measured in weld regions

Heat input affects the occurrence of defects. Too low heat input (excessive welding speed or insufficient power) can cause insufficient penetration and the formation of pores in the weld joint [Moeinifar 2011, Bagger 2005]. The heat input usually has a detrimental effect on the mechanical properties of the welded joint [Pouranvari 2011]. The increased volume fraction of martensite in the welded joint contributes to a decrease in ductility and an increase in hardness and strength – Fig. 9. The hardness strongly depends on the carbon content and on the cooling rate. The higher the welding speed, the higher the cooling rate [Hilditch 2007, Moeinifar 2011]. Lower speed promotes weld penetration but increases heat dissipation in the transverse direction of the weld, resulting in wider welds.

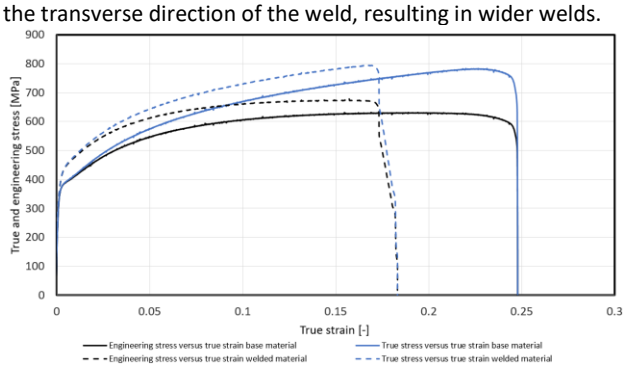

Figure 9. Comparison of stress-strain curves (engineering and true) of the base material and welded one.

Based on simulated thermal cycles and material properties, Sysweld can estimate the proportion of phases present after the weld is completed in the different areas of the welded joint - Fig. 10. and Fig. 11 As mentioned above, due to the high cooling rates, austenite is converted to martensite. It should be noted that the portion of martensite indicated by the simulation only includes the martensite transformed during welding, not including the pre-existing martensite from the base metal. The base material is equivalent to the material in the as-delivered state, composed of ferrite and martensite. In the FZ area, the proportion of martensite reaches 100% and

gradually decreases to about 18-20% of the base material. These estimates are in good agreement with the findings in the metallographic samples of Fig. 7a-7b. It should be noted that at the HAZ and BM boundary the phase composition is close to the base material. The martensite fraction of 0% for BM is incorrectly evaluated. We supposed it is due to temperature field is under the temperature of phase transformation.

This situation is the same for both computational variants. Thus, despite some difference in the welding speed and in the cooling rates of the material behind the heat source, the resulting size of the HAZ and the type of microstructure within it are virtually identical.

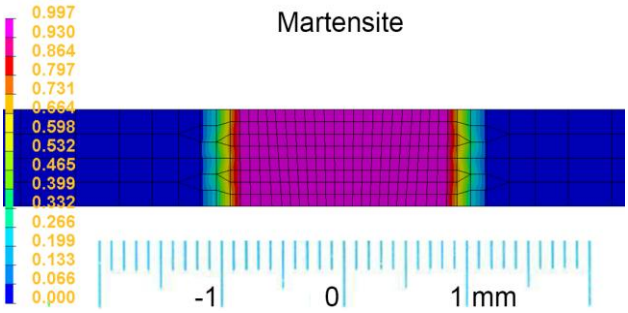

Figure 10. The proportion of martensite in the weld metal at the welding speed V1.

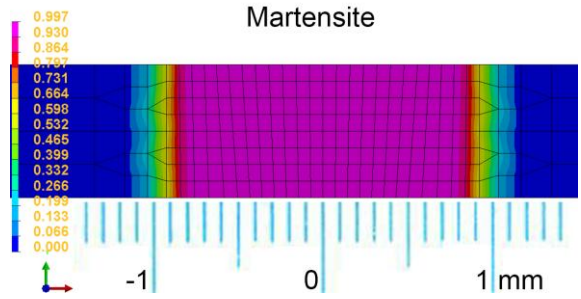

Figure 11. The proportion of martensite in the weld metal at the welding speed V2.

This is confirmed by the hardness calculation results showing the distribution of hardness values at the mid-section of the model and the graph in Fig. 12, which shows the hardness profiles along the mid-section plane. Figure 12 shows that the HAZ at welding speed V1 is identical to that at welding speed V2. The resulting hardness of the martensitic structure inside the HAZ reaches a maximum value of 395 HV and 396 HV for the V01 and V02 variants, respectively. We note that the hardness value of 210 HV in the base material region is to be understood as an initial condition input rather than as a direct output of the calculation. In practice, microhardness and other initial material properties are the result of the sheet metal fabrication process. Thus, the exact material in this case was not even directly represented.

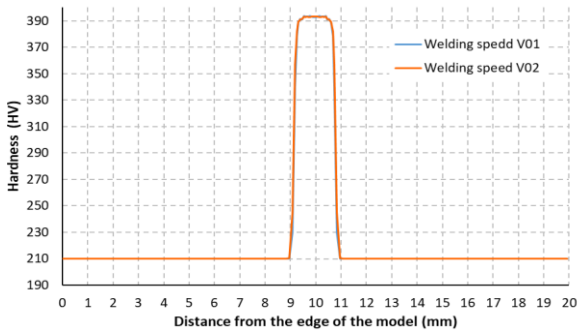

Figure 12. Comparison of hardness and weld area widths at welding speeds V1 and V2.

The results of the mechanical analysis of the welding process show that the von Mises residual stresses at the end of the process, i.e. after welding and cooling to ambient temperature, are very similar for both variants - Fig. 13 to Fig. 15. In the region between the FZ and the HAZ, these stresses reach a level of 500 MPa according to Mises, i.e. they exceed the average value of the yield stress (376 MPa). Compared to the value of the yield strength of the base material, the values of the yield strength inside the TOO are greater by approx. 850 MPa –Fig. 16. This indicates that welding generates plastic deformation in the weld area, because martensite has a much higher strength than that of the base material. In the HAZ region the stress levels reach values over 100 MPa, i.e. lower than the yield strength. This apparently can be attributed to the martensitic transformation, apparently this is associated with volume expansion.

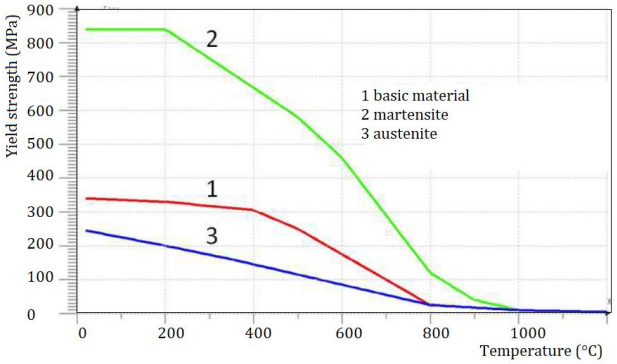

Figure 16. Yield strength of individual phases in MPa of DP-W-600 steel

The reported values of residual stresses and plastic strains are expressed in terms of actual stress and strain values. This is a logical consequence of the fact that even at the level of the initial definition of material properties (strain hardening curves for the elastoplastic material model), the expression in actual values is again used exclusively. Fig. 14 shows the distribution of the cumulative plastic strain. This quantity has the meaning of the equivalent plastic strain registered in the alpha phase of the material.

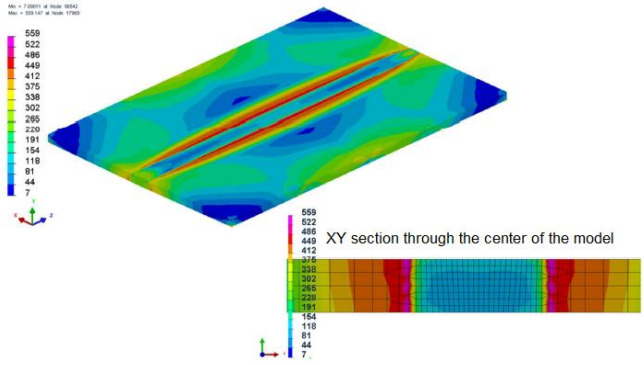

Figure 13a. Von Mises residual stresses after specimen cooling - variant V1.

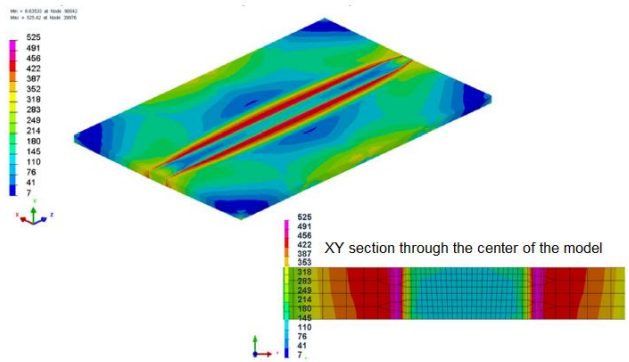

Figure 13b. Von Mises residual stresses after specimen cooling: (a) variant V2.

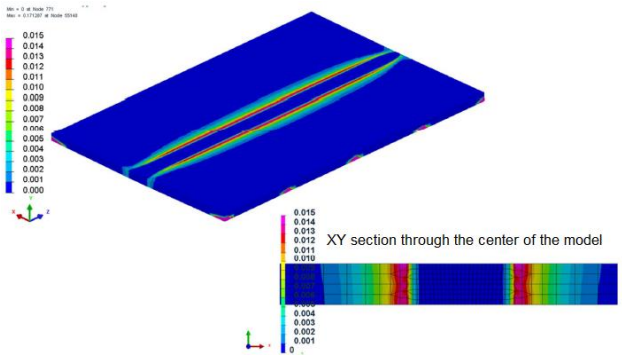

Figure 14a. Strains after specimen cooling -variant V1.

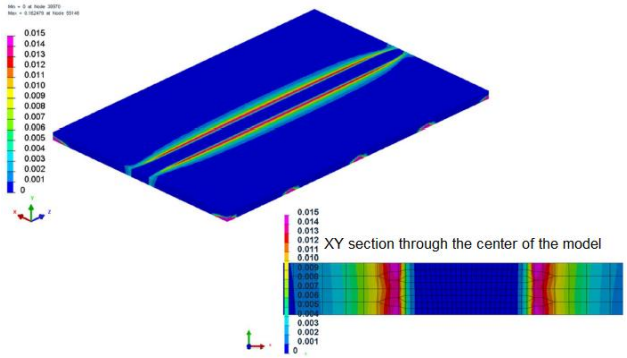

Figure 14b. Strains after specimen cooling -variant V2.

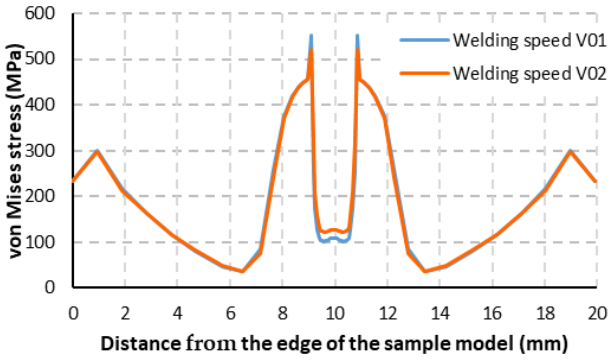

Figure 15a. Mechanical analysis at welding speeds V1 and V2 - residual stress.

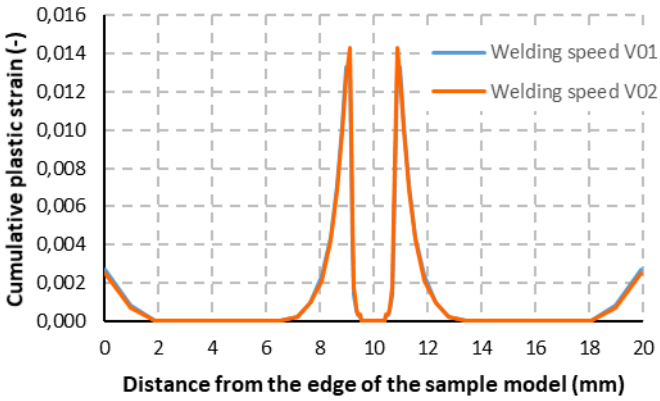

Figure 15b. Mechanical analysis at welding speeds V1and V2 – strains.

Fig. 17 presents the state in terms of the resulting distortions of the model (bias field). It can be concluded that neither the course nor the values of the two computational variants differ in any fundamental way. In terms of absolute values, the resulting deviations are small. However, in principle, it is possible to observe, for example, the effect of transverse shrinkage of the sample, which is most pronounced in the middle region of the sample (longitudinally), where it reaches a total size of about 0.1 mm, while at the ends of the sample it is practically zero. The resulting angular deformation of the sample is also evident. Here, on the other hand, the deflection line is meant to be fairly constant along the entire specimen and, with the considered support at the lateral edges of the specimen, then the transverse deflection in the middle of the in the weld area is about 0.1 mm.

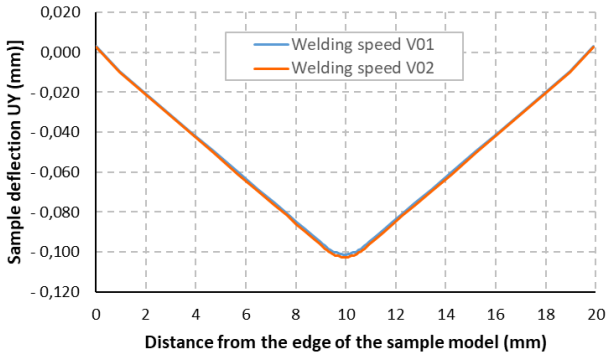

Figure 17. Comparison of specimen deflections at welding speeds V1 and V2.

4. CONCLUSIONS

The intention of the paper was to perform a numerical analysis of the laser welding process of a 0.78 sheet metal specimen made of HCT600X material using the SYSWELD finite-element solver. Within the numerical experiment, calculations were performed and the results were compared for two variants of the process parameters:

- V1 - power input 2 kW, welding speed 50 mm/s
- V2 - power input 2.7 kW, welding speed 70 mm/s.

The simulation in the SYSWELD solver was aimed at studying the processes in the solid phase of the material induced by the thermal effects of the welding process. It was mainly a non-stationary analysis of the heat conduction problem in the material coupled with the analysis of the problem of phase transformations (especially solid state transformations) and the corresponding mechanical response of the simulation model.

Emphasis was placed on advanced and strongly nonlinear material models, which allow to describe the changes in material properties due to changes in temperature and phase or microstructural transformations in the material associated with the temperature history induced by the process. Following outputs were found:

- very similar situation in both computational variants in terms of the nature and penetration of the temperature fields around the welded joint was found - in variant 2 (higher power and welding speed) a slightly "narrower" temperature field resulted in slightly higher heating and cooling rates can be observed in total for variant 2. However, differences between these results are very small and, from a practical point of view, insignificant. Thus, very similar weld widths was found.
- In the experiment the total width of the weld joint is approx. 2 mm, the width of welded metal area is approx. 1.2 mm and the width of heat-affected area is approx. 0.4 mm.
- in numerical simulation the total width of the weld joint is approx. 2.3 mm, the width of welded metal area is approx. 1.6 mm and the width of heat-affected area is approx. 0.3 mm.
- microhardness in weld metal was 388.6 ± 5 HV0.5 measured in experiment and it was 393.6 HV0.5 for V1 and 393.1 HV0.5 for V2 determined by numerical simulation.

The representation of the heat input of the welding process was made based on the definition of an equivalent heat source, with the help of which an identical temperature field to that of the real weld was induced in the model. When the heat source was specified, the net power input to the material was defined, thereby controlling the parameters that govern the spatial distribution of the power density and that result in the desired character of the temperature field. Thus, it is the calibration of the heat source that is typically performed based on knowledge of the actual process parameters and the corresponding weld macrography.

ACKNOWLEDGMENTS

The work was accomplished under the grant project VEGA 1-0238-23 “Implementation of CAx systems and virtual engineering techniques in the redesign of car-body parts for deformation zones”.

References

[Alves 2018] Alves, P.H.O.M., Lima, M.S.F., Raabe, D., Sandim, H.R.Z. Laser beam welding of dual-phase DP1000 steel. Journal of Materials Processing Technology, February 2018, Vol. 252, pp 498-510.

[Bagger 2005] Bagger, C., Olsen, F.O. Review of laser hybrid welding. Journal of Laser Applications, 2004, Vol. 17, No. 1., pp 2-14.

[Beer 2020] Beer, F., Johnston, R., Dewolf, J, Mazurek, D. Mechanics of Materials. 8th Edition. New York: McGraw-Hill, 2020. ISBN 9781260569971.

[Bergman 2011] Bergmann, J.P., Patschger, A., Bastick, A. Enhancing Process Efficiency due to high Focusing with high Brightness Lasers – Applicability and constraints. Physics Procedia, 2011, No. 12., pp. 66–74.

[Correard 2016] Correard, G.C.C., Miranda, G.P., Lima, M.S.F. Development of laser beam welding of advanced high-strength steels. Int. J. Adv. Manuf. Technol. 2016, 83/9–12, pp 1967–1977.

[Danielewski 2020] Danielewski, H., Skrzypczyk, A. Steel Sheets Laser Lap Joint Welding—Process Analysis. Materials, May 2020, Vol. 13, 2258.

[Devaraj 2021] Devaraj, J., Ziout, A., Abu Qudeiri, J.E. Dissimilar Non-Ferrous Metal Welding: An Insight on Experimental and Numerical Analysis. Metals, 2021, Vol. 11, 1486.

[Dong 2014] Dong et al. Microstructure and dynamic tensile behavior of DP600 dual phase steel joint by laser welding. Materials Science and Engineering: A, January 2014, Vol. 594, No. 31., pp 17-25.

[Doshi 2020] Doshi, S., Jani, D.B., Gohil, A.V., Patel, C.M. Progress in the arc plasma temperature measurement and its finite element analysis in pulsed MIG welding process. Materials Today, 2020, Vol. 38, No. 5., pp 2745-2750.

[Evin 2017] Evin, E.; Tomas, M. The Influence of Laser Welding on the Mechanical Properties of Dual Phase and Trip Steels. Metals, June 2017, Vol. 7, No. 7., 239.

[Farabi 2010] Farabi, N., Chen, D.L., Li, J., Zhou, Y., Dong, S.J. Microstructure and mechanical properties of laser welded DP600 steel joints. Materials Science Engineering: A, February 2010, Vol. 527, No. 4.–5., pp 1215–1222.

[Gao 2018] Gao, S., Gao, Y., Li, Y., Yang, L., Qiu, W. Microstructure and mechanical properties of laser-welded dissimilar DP780 and DP980 high-strength steel joints. Materials Science and Engineering: A, March 2018, Vol.720, No. 21., pp 117-129.

[Hilditch 2007] Hilditch, T.B., Speer, J.G., Matlock, D.K. Effect of susceptibility to interfacial fracture on fatigue properties of spot-welded high strength sheet steel. Materials & Design 2007, Vol. 28, No. 10., pp 2566-2576.

[Kik 2020] Kik, T., Moravec, J., Svec. Experiments and Numerical Simulations of the Annealing Temperature Influence in the Residual Stresses Level in S700MC Steel Welded Elements. Materials, November 2020, Vol. 13, No. 22., 5289.

[Mansur 2021] Mansur, M., et al. Effect of laser welding on microstructure and mechanical behaviour of dual phase 600 steel sheets. Heliyon, December 2021, Vol. 7, No. 12., e08601.

[Moeinifar 2011] Moeinifar, S.; Kokabi, A.H.; Hosseini, H.R.M. Role of tandem submerged arc welding thermal cycles on properties of the heat affected zone in X80 microalloyed pipe line steel. Journal of Materials Processing Technology, March 2011, Vol. 211, No. 3., pp 368-375.

[Pouranvari 2011] Pouranvari, M.; Mousavizadeh, S.M.; Marashi, S.P.H.; Goodarzi, M.; Ghorbani, M. Influence of fusion zone size and failure mode on mechanical performance of dissimilar resistance spot welds of AISI 1008 low carbon steel and DP600 advanced high strength steel. Materials & Design, March 2011, Vol. 32, No. 3., pp 1390-1398.

[Rusz 2019] Rusz, S., Hilser, O., Ochodek, V., Cada, R., Svec, J., Szkandera, P. Influence of SPD process on low-carbon steel mechanical properties. MM Science Journal, June 2019, pp 2910-2914.

[Schindlerova 2024] Schindlerova, V., Marcik, J., Cada, R., Sajdlerova. I. Analysis of Non-Conforming Production in an Engineering Company. Tehnicni vjesnik, 2024, Vol. 31, No. 1, pp 296-302.

[Schmitt 2018] Schmitt, J.H., Iung, T. New developments of advanced high-strength steels for automotive applications. Comptes Rendus Physique, December 2018, Vol. 19, No. 8., pp 641-656.

[Sokolov 2014] Sokolov, M., Salminen, A. Improving Laser Beam Welding Efficiency. Engineering, July 2014, No. 6., pp. 559-571.

[Stańczyk 2023] Stanczyk, M. Influence of the Quality of Metal Sheet Edges After Strip Slitting Processes in Integrated Lines on the Quality of Laser Welds.

Advances in Science and Technology Research Journal, 2023, Vol. 17, No. 2., pp 136-146.

[Sternadelova 2023] Sternadelova, K., Krupova, H., Matysek, D., Mohyla, P. Quality Assessment of the Vitreous Enamel Coating Applied to the Weld Joint. MM Science Journal, March 2023, pp 6333 -6338.

[Svec 2018] Svec, P.; Schrek, A.; Domankova, M. Microstructural characteristics of fibre laser welded joint of dual phase steel with complex phase steel. Kovove Materialy - Metallic Materials, February 2018, Vol. 56, No. 1., pp 29-40.

[Vrtiel 2019] Vrtiel, S., Behulova, M. Analysis of Temperature and Stress-Strain Fields during Laser Beamwelding of a TRIP Steel In: Development of Materials Science in Research and Education (DMSRE29 Nova Lesna: 02-06 September, 2019. OP Conf. Series: Materials Science and Engineering, 2020, Vol 726, ISSN: 1757-8981.

[Xu 2016] Xu, P., Yang, C., Peng, Y., et al. Crash performance and multi-objective optimization of a gradual energy absorbing structure for subway vehicles. International Journal of Mechanical Sciences, March 2016, Vol. 107, pp 1-12.

[Zhao 2013] Zhao, Y.Y., Zhang, Y.S., Hu, W. Effect of welding speed on microstructure, hardness and tensile properties in laser welding of advanced high strength steel. Science and Technology of Welding and Joining, December 2013, Vol. 18, No. 7., pp 581–590.

CONTACTS:

prof. Ing. Emil Evin,CSc.
Department of Automotive Production, Faculty of Mechanical Engineering, Technical University of Kosice, Mäsiarska 74, 040 01 Kosice, Slovakia; emil.evin@tuke.sk, https://www.sjf.tuke.sk/kav/sk/home-mainmenu-2/pracovnici-katedry

doc. Ing. Miroslav Tomas, PhD.
Department of Automotive Production, Faculty of Mechanical Engineering, Technical University of Kosice, Mäsiarska 74, 040 01 Kosice, Slovakia; miroslav.tomas@tuke.sk, https://www.sjf.tuke.sk/kav/sk/home-mainmenu-2/pracovnici-katedry

Ing. Josef Tejc
ESI Eastern Europe s.r.o, Brojova 2113/16, 326 00 Plzen, Czech republic; josef.tejc@esi-group.com, www.esi-group.com

Ing. Vladimir Kokarda
Carl Zeiss Slovakia, s.r.o, Racianska 1481/77/A, 831 02 Bratislava 3, Slovakia; vladimir.kokarda@zeiss.com; www.zeiss.sk